Materials Transactions, Vol. 66, No. 8 (2025) pp. 1006 to 1013

Effect of Porosity on High Temperature Compressive Behavior of Textured Ti_3SiC_2 Bodies Prepared by Pressureless Sintering*1

Eiichi Sei[1,*2], Ken-ichi Ikeda[2,*3], Seiji Miura[2], Koji Morita[3], Tohru S. Suzuki[3] and Yoshio Sakka[3]

[1]*Division of Materials Science and Engineering, Graduate School of Engineering, Hokkaido University, Sapporo 060-8628, Japan*
[2]*Division of Materials Science and Engineering, Faculty of Engineering, Hokkaido University, Sapporo 060-8628, Japan*
[3]*National Institute for Materials Science, Tsukuba 305-0047, Japan*

To clarify the effect of pores on high temperature compressive behavior due to kink deformation, textured Ti_3SiC_2 pressureless sintered bodies were fabricated and examined by high temperature compression tests with different porosities.

The textured Ti_3SiC_2 pressureless sintered bodies were prepared by slip casting in a strong magnetic field and spark plasma sintering at 1400°C for 1 h. Samples were cut into rectangular shape with 45° between the casting direction and the compression axis, and compression tests were conducted at 1200°C at a strain rate of $3 \times 10^{-4}\,s^{-1}$. Porosity was evaluated by Archimedes method and binarization. Crystal orientation analysis using EBSD method was performed to observe the microstructure evolution before and after the compression test.

The sintered bodies had a strongly textured microstructure with homogeneous dispersed pores. The results of high temperature compression tests showed that the 0.2% proof stress depended on the porosity before compression tests. On the other hand, the work hardening coefficient was larger for plessureless sintered sample with high porosity, which attributed to the densification associated with the compression. Microstructural observations indicated that fine kink bands formed in the middle stage of the compression and then disappeared, suggesting that this is important for clarifying kink-band strengthening in the MAX phase. [doi:10.2320/matertrans.MT-M2025063]

(Received April 22, 2025; Accepted May 15, 2025; Published July 25, 2025)

Keywords: *Ti_3SiC_2, kink deformation, texture, porosity, high temperature deformation*

1. Introduction

MAX phases are ternary compounds with the general formula $M_{n+1}AX_n$ (M: early transition metal, A: A-group element, X: C or N, n = 1–3). They are unique materials with metallic (high thermal/electrical conductivity and machinability) and ceramic (low density, high rigidity, and oxidation resistance) properties [1–3]. Ti_3SiC_2 is one of the most extensively studied MAX phases; it has a hexagonal layered crystal structure ($a = 0.3067$ mm, $c = 1.767$ mm) [1], in which Ti-C and Si layers are stacked along the *c*-axis. Therefore, it exhibits anisotropic properties [4–6] and basal slips as the predominant plastic deformation mechanism.

Kink deformation is one of the deformation mechanisms in layered materials. It has been confirmed in Cd [7], Zn [8], graphite [9], mica [10], polymers [11], and MAX phases [12–16]. Barsoum and El-Raghy [13] demonstrated that kink deformation occurred in textured Ti_3SiC_2 when the compression axis was perpendicular to the *c*-axis. Shirakami *et al.* [6] have also performed compression tests on textured Ti_3SiC_2 at 1200°C and found that kink deformation was more pronounced when the angle between the compression axis and *c*-axis was 90° than when it was 0° or 45°. In addition, Matsui *et al.* [14, 15] evaluated the microstructure of Ti_3SiC_2 polycrystals after high temperature compressive creep tests and reported that kink deformation occurred more frequently in grains whose orientation differed from the compression axis to the basal planes by within 10°. In contrast, Higashi *et al.* [16] have reported that kink deformation in Ti_3SiC_2 single crystals occurs only when the compression direction is perpendicular to the *c*-axis ($[\bar{1}2\bar{1}0]$ or $[\bar{1}100]$), as shown by room temperature micropillar compression tests.

Kink-band strengthening has recently been proposed as a new strengthening mechanism, because kink bands, which are deformation bands formed by kink deformation, act as obstacles to dislocation motion. This was first reported in Mg-Zn-Y alloys with a long-period stacking ordered (LPSO) structure. For Mg alloys, Kawamura *et al.* [17, 18] performed tensile tests on specimens with kink bands introduced by hot extrusion and found that mechanical strength (e.g., 0.2% proof stress) improved via the kink-band strengthening. Somekawa *et al.* [19] concluded that kink boundaries with angles of 20° or more hinder dislocation motion. Kink deformation and kink-band strengthening at room temperature have also been confirmed in Al-Cu eutectic alloys [20].

Although kink-band strengthening has been observed in Mg/LPSO and Al-Cu alloys, it remains scarce in the MAX phases. One reason is that delamination, as well as the residual pores formed during sintering, significantly affects the mechanical properties. Hashimoto *et al.* [21, 22] investigated the effects of grain restriction on kink deformation by performing high temperature compression tests on textured Ti_3SiC_2 dense and porous samples. They found that a weaker constraint promoted more crystal rotation. The porous sample had a porosity difference of approximately 10 vol%. Therefore, to understand the strengthening mechanism of Ti_3SiC_2, it is necessary to fabricate samples with uniformly dispersed pores and to investigate the relationships among mechanical properties, porosity, and kink deformation bands.

As mentioned preciously, the relationship between the crystallographic orientation and compression direction is crucial for kink deformation. Therefore, alignment control simplifies the observation of kink deformation behavior [6, 21, 22]. Tape-casting [23] and hot-pressing [24] are common texturing techniques for ceramics; however, it is difficult

*1This Paper was Originally Published in Japanese in J. Japan Inst. Met. Mater. **88** (2024) 297–305.

*2Graduate Student, Hokkaido University
*3Corresponding author, E-mail: ikeda.ken-ichi@eng.hokudai.ac.jp

to control the shape of the compacts and their orientation direction. Therefore, slip casting in a strong magnetic field (SCMF) [25, 26] was conducted. Slip casting is a process in which raw powder is mixed with a liquid to prepare a slurry, which is then poured into a porous mold to remove the solvent. Textured Ti_3SiC_2 was obtained through SCMF at 12 T [4–6, 21, 22, 27–29].

This research has two objectives. The first is to fabricate textured Ti_3SiC_2 with uniformly dispersed pores and to evaluate its microstructure. The second is to investigate how high temperature compressive behavior, porosity, and microstructure are related to kink deformation.

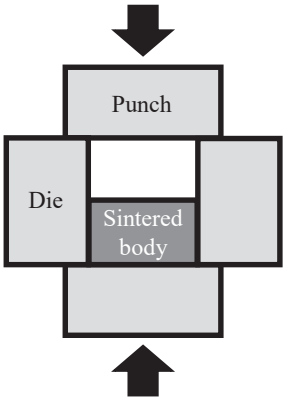

Fig. 1 Schematic image of the pressureless sintering.

2. Experimental Procedures

2.1 Slurry preparation

First, commercial Ti_3SiC_2 powder (Maxthal (312), KANTHAL, particle size: 1–10 μm) was mixed with ethanol as a solvent, maintaining a powder content of 30 vol%. Polyethyleneimine (PEI, FUJIFILM Wako Pure Chemical Corp.) was then added as a dispersant to prevent powder agglomeration in the slurry. The PEI content was 1.5 mass% relative to the Ti_3SiC_2 powder. The slurry was redispersed using an ultrasonic homogenizer (GSD-600AT, Sonic Technology Inc.) while stirring at room temperature, and then defoamed by stirring under vacuum for 10 min.

2.2 Fabrication of textured Ti_3SiC_2 sintered body

Green bodies were prepared by slip casting of the slurry in a rotating magnetic field. First, a porous alumina mold was covered with a membrane filter with a pore diameter of 0.2 μm; the slurry was then poured into the acrylic pipes (diameter: 25 mm, height: 30 mm) placed on the mold. A release film composed of polyethylene terephthalate was attached to the inner walls of each pipe. Next, the mold was rotated at 20 rpm in a superconducting magnet (JMTD-12T1-NC5, JASTEC), and a strong magnetic field of 12 T was applied perpendicular to both the casting direction and rotating axis. This aligned the *c*-axis parallel to the casting direction. After that, cold isostatic pressing was performed at 350 MPa for 10 min.

Sintered bodies were obtained using a spark plasma sintering (SPS) machine (SPS-510L, Fuji Electronic Industrial Co.). In general, SPS is a sintering method using uniaxial pressing force and the Joule heat via DC pulse current. However, to preserve the pores, pressureless sintering [21, 22] was performed using a punch with a diameter larger than the inner diameter of the die, as shown in Fig. 1. The sintering process proceeded as follows: first, under vacuum, the body was heated at 600°C for 10 min to burn out the PEI. After restoring the vacuum, the atmosphere was replaced with argon. It was then heated at a rate of 50°C/min and held at 1400°C for 1 h. For comparison, the textured dense body was sintered at 1300°C for 10 min under a uniaxial compressive pressure of 40 MPa.

2.3 Evaluation of textured pressureless-sintered body

The porosities of the sintered bodies were calculated using the Archimedes method with kerosene as the solvent. Phase composition and grain orientation were evaluated by X-ray diffraction (XRD, Smart Lab, Rigaku) using Cu(Kα1) radiation. The samples were cut on planes parallel and perpendicular to the casting direction and polished with emery paper. These surfaces are referred to as the "side" and "top" surfaces, respectively.

The side surface was mirror-polished with emery paper, diamond film, and diamond slurry, and then backscattered electron (BSE) images were obtained with field-emission scanning electron microscope (FE-SEM, JSM-7001FA, JSM-7200F, JEOL Ltd.). Moreover, the side surface was additionally polished with colloidal silica (particle size: 0.04 μm) and analyzed by electron backscattered diffraction (EBSD) with FE-SEM (JSM-6500F, JEOL Ltd./OIM Data Collection, TSL Solutions, Inc.).

2.4 High temperature compression test and microstructure evaluation

The samples were cut from a textured dense body and from two pressureless-sintered bodies with different porosities. Their dimensions were 1.5 mm × 1.5 mm × 2.25 mm, and the *c*-axis of the crystal was oriented 45° relative to the compression axis. Hereafter, they are referred to as "Dense", "Low-porosity", and "High-porosity" samples. The top and bottom surfaces of each sample were polished with emery paper, and the side surfaces were mirror-polished.

Compression tests were performed with an Instron 8562 universal testing machine. Boron nitride was sprayed on the sample and on the ground surface of the machine. The machine was heated to the testing temperature of 1200°C at a rate of 15°C/min, and tests were then conducted at a strain rate of $3 \times 10^{-4}\,s^{-1}$, under 4×10^{-4} Pa. Two of each sample were compressed to consider the influence of porosity and microstructure on deformation behavior, with final strains of approximately 10% (intermediate deformation) and 20% (large deformation).

EBSD analysis and BSE imaging were conducted before and after compression. The side surface of each sample was analyzed before compression. After compression, a plane cut parallel to the compression axis was mirror-polished and evaluated. The obtained BSE images were binarized using ImageJ (NIH) software, and the porosity was calculated. Binarization was employed because the small sample size led to large errors in the Archimedes method. In these sample, porosity calculated using the Archimedes method was 1.7 times higher than the value obtained via binarization.

3. Results and Discussions

3.1 Microstructure evaluation of the textured pressureless-sintered body

A textured pressureless-sintered body with a porosity of 6.5%, measured by the Archimedes method, was evaluated. Figure 2 shows the XRD patterns of the raw powder, side surface, and top surface. The bold italicized indices indicate that the peaks were derived from the (000*l*) planes of Ti_3SiC_2, whereas TiC is indicated by open symbols. On the side surface, strong peaks corresponding to the (*hkil*) planes ($2\theta = 33.9°$, 60.2°) were observed, while peaks arising from the (000*l*) planes ($2\theta = 30.2°$, 40.7°) were observed on the top surface. This suggests that the *c*-axes of the body were highly aligned in the slip casting direction.

To quantitatively analyze the texturing, the Lotgering factor (f_L) was calculated using eqs. (1) and (2):

$$f_L = \frac{P - P_0}{1 - P_0} \tag{1}$$

$$P = \frac{\sum I_{(000l)}}{\sum I_{(hkil)}} \tag{2}$$

where P is the ratio of the sum of the diffraction intensities derived from the (000*l*) and (*hkil*) planes, and P_0 is the P value for a reference sample (the raw powder). The f_L value ranges from 0 to 1, where 1 represents perfect texturing. The f_L of the textured pressureless-sintered body was 0.95, indicating strong orientation. This is agreed with the fact that a textured dense sample with sufficient texturing has an f_L value of 0.90.

The results of the crystal orientation analysis and BSE images are shown in Fig. 3. Figure 3(a) shows an inverse pole figure (IPF) map based on the color key in Fig. 3(b). Figure 3(a) shows the plate-like grains, which are 2–7 μm on the short side and 10–25 μm on the long side. Moreover, the 0001 pole figure (PF) in Fig. 3(c) shows that the *c*-axis of the crystal is concentrated along the y-axis, which is the casting direction.

Kinked grains are observed in the IPF maps (red arrows in Fig. 3(a)). The sintering temperature (1400°C) is higher than 1100–1200°C, the brittle-ductile transition temperature of Ti_3SiC_2 [30, 31]. Therefore, it is assumed that the kinked grains formed due to the reaction force of the die against the thermal expansion of the sintered body. The black areas correspond to regions of poor crystallinity (white arrows in Fig. 3(a)), which are usually grain boundaries, different phases, and/or strain. However, these pores appeared to have been introduced by the sintering process, as the black areas were round and evenly distributed in the observed area. A

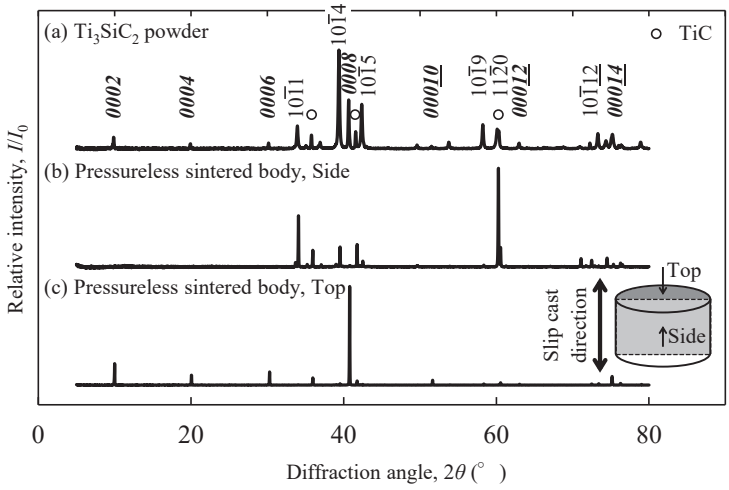

Fig. 2 X-ray diffraction patterns of (a) Ti_3SiC_2 powder and the sintered body taken from (b) side surface and (c) top surface.

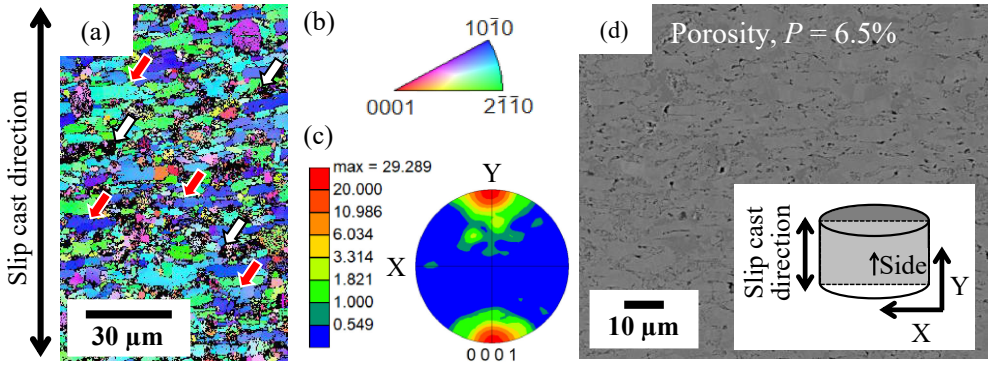

Fig. 3 (a) Inverse pole figure (IPF) map of the sintered body and (b) its color-coded map. The red and white arrows in (a) show kinked grains and pores, respectively. (c) 0001 pole figure (PF) of (a). (d) BSE image of the textured microstructure. (a) and (d) are taken from side surface. (online color)

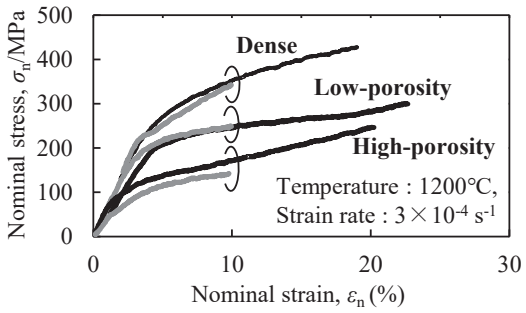

Fig. 4 Compressive stress-strain curves of samples tested at 1200°C.

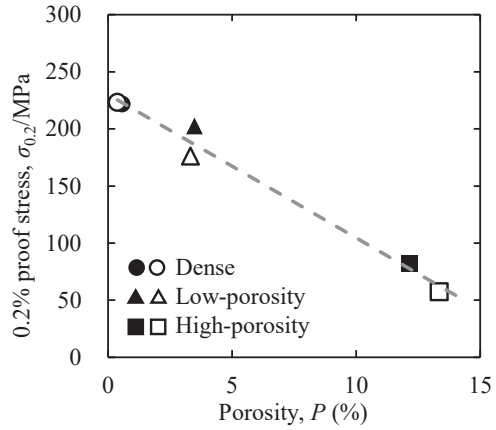

Fig. 5 Relationship between the 0.2% proof stress and porosity before the compression measured by binarization. The open symbols are the values of intermediate samples.

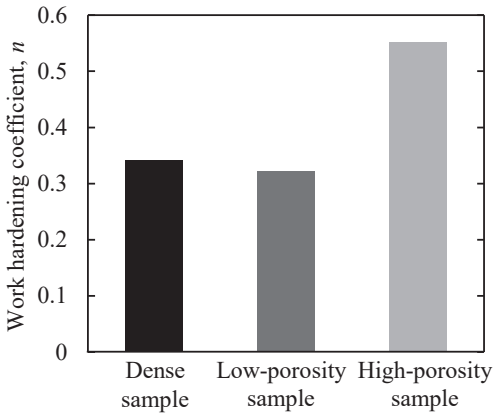

Fig. 6 Average values of work hardening coefficient of samples.

Table 1 Porosity of samples before and after the compression measured by binarization.

		Porosity before the compression (%)	Porosity after the compression (%)
Dense sample	$\varepsilon \doteqdot 10\%$	0.57 ± 0.24	0.29 ± 0.16
	$\varepsilon \doteqdot 20\%$	0.38 ± 0.19	0.30 ± 0.20
Low-porosity sample	$\varepsilon \doteqdot 10\%$	3.49 ± 0.64	5.89 ± 1.75
	$\varepsilon \doteqdot 20\%$	3.32 ± 0.38	5.49 ± 1.49
High-porosity sample	$\varepsilon \doteqdot 10\%$	12.18 ± 1.42	6.12 ± 1.28
	$\varepsilon \doteqdot 20\%$	13.35 ± 1.03	10.25 ± 0.95

uniform distribution of pores was also observed in the BSE image (Fig. 3(d)), confirming that the initially intended pore residue was achieved.

3.2 High temperature compression test

Figure 4 shows the nominal stress-strain curves of the Dense, Low-porosity, and High-porosity samples. This deformation behavior is consistent with the results of previous study [13]. The 0.2% proof stresses were 221.8 MPa, 202.4 MPa, and 81.9 MPa for the Dense, Low-porosity, and High-porosity samples. Figure 5 shows the relationship between the 0.2% proof stress and porosity before compression. The stress decreased linearly with increasing in porosity. Equations (3) and (4) describe the porosity dependence of the mechanical strength in ceramics and cermets [32–35]:

$$\sigma = \sigma_0 D^m \tag{3}$$

$$\sigma = \sigma_0 \exp(-kP) \tag{4}$$

where σ is the strength of a porous material, σ_0 is the strength of a non-porous material, D $(= 1 - P)$ is a relative density, P is a porosity, and m and k are constant of 3 or greater. The strength of the materials decreases exponentially with increasing porosity, and this effect becomes more pronounced once the porosity exceeds 20%. The results in Fig. 5 are reasonable because the porosity range of these samples (approximately 0.4–13.5%) can be regarded as sufficiently linear.

Figure 6 shows the average work-hardening coefficients (n) for two of each compression test. These values were calculated in the strain range that could be approximated by eq. (5) from the yielding point:

$$n = \frac{\mathrm{d}(\ln \sigma_t)}{\mathrm{d}(\ln \varepsilon_t)} \tag{5}$$

where σ_t is the true stress and ε_t is the true strain. These coefficients are generally used to evaluate machinability (e.g., bulging and drawing). However, n-values were used as indices to quantitatively compare the work hardening, regarded as the stress ($\mathrm{d}(\ln \sigma_t)$) required to obtain a certain strain ($\mathrm{d}(\ln \varepsilon_t)$). The value for the High-porosity sample was 0.55, whereas the Dense and Low-porosity samples exhibited n-values of 0.34 and 0.32, respectively.

This difference is attributed to changes in porosity during deformation. The porosity obtained by binarization before and after compression are listed in Table 1. The porosities of the Dense and Low-porosity samples decreased slightly, whereas a substantial decrease was observed in the High-porosity samples. These results indicate that densification by plastic deformation increases the deformation stress. The compression behavior of porous metals can be divided into elastic, plateau, and densification regions, but the distinction becomes less clear with decreasing porosity, as the deformation stress increases immediately after yielding [36–38].

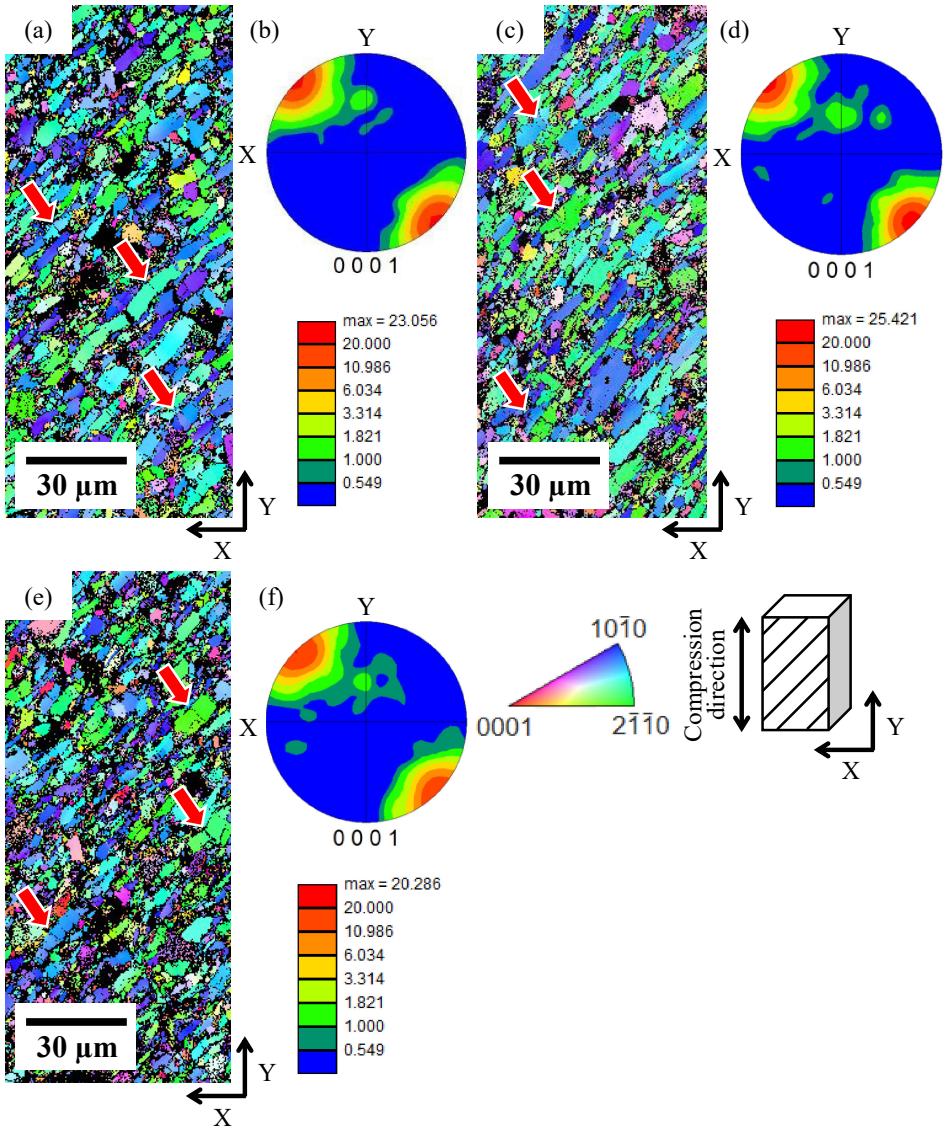

Fig. 7 (a), (c), (e) IPF maps and (b), (d), (f) 0001 PFs. These figures are obtained in (a), (b) Dense, (c), (d) Low-porosity sample, and (e), (f) High-porosity sample before the compression. The red arrows in IPF maps indicate kinked grains. (online color)

3.3 Microstructure evaluation before and after compression

Figures 7 and 8 show the IPF maps and 0001 PFs before and after compression, respectively. Note that the IPF maps in Fig. 8 are magnified images compared with those in Fig. 7. Kinked grains were frequently observed after large deformation, which agrees with previous work [6]. The maximum intensity for each sample decreased through compression because kink deformation induced crystallographic misorientation within single grains. However, considering that the compression axis was at 45° from the *c*-axis, dislocation slips are likely, whereas kink deformation is unlikely. This is assumed to be due to the presence of numerous pores and impurities in the polycrystal samples.

Figure 9 shows an example of the kink deformation band analysis used to understand the compression behavior. First, the kinked grains were extracted from the IPF maps (Fig. 9(a)), and rotation angle profiles (Fig. 9(b)) were generated by measuring the crystal misorientation between each pixel and the starting pixel. Second, approximately 200 kink boundaries were measured under the following conditions: (1) the rotation axis was perpendicular to the *c*-axis, and (2) the angle change was sharp.

Table 2 summarizes the variation in the average number of kink boundaries and average angle of the kink boundaries. The average number of kink boundaries was calculated by dividing the total number of kink boundaries by the number of extracted grains (i.e., number of kink boundaries per grain). The average number of kink boundaries increased for the Dense and Low-porosity samples, meanwhile the average angle of the kink boundaries decreased for all samples. This trend is attributed to the formation of kink boundaries with small angles. Figure 10 shows histograms of kink boundary angles for the Dense samples before and after compression. Regardless of the final strain, the distribution shifted toward the smaller angles, and the fraction of kink boundaries below 10° increased. Such formation of kink deformation bands produces dislocation-dislocation and dislocation-kink boundary interactions, influencing the compressive behavior.

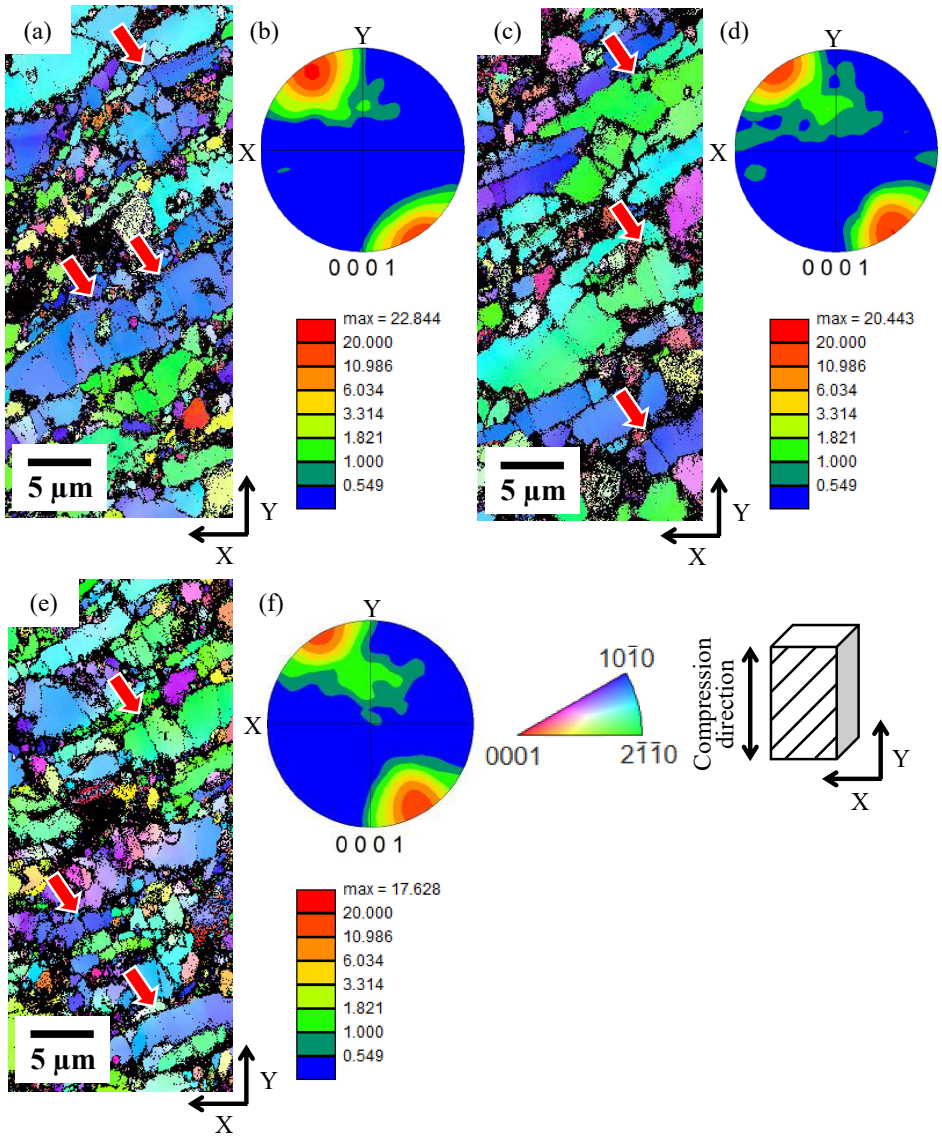

Fig. 8 (a), (c), (e) IPF maps and (b), (d), (f) 0001 PFs obtained in (a), (b) Dense, (c), (d) Low-porosity sample, and (e), (f) High-porosity sample after the compression up to 20% strain. Note that only IPF maps are magnified images compared to Fig. 7. The red arrows in IPF maps indicate kinked grains. (online color)

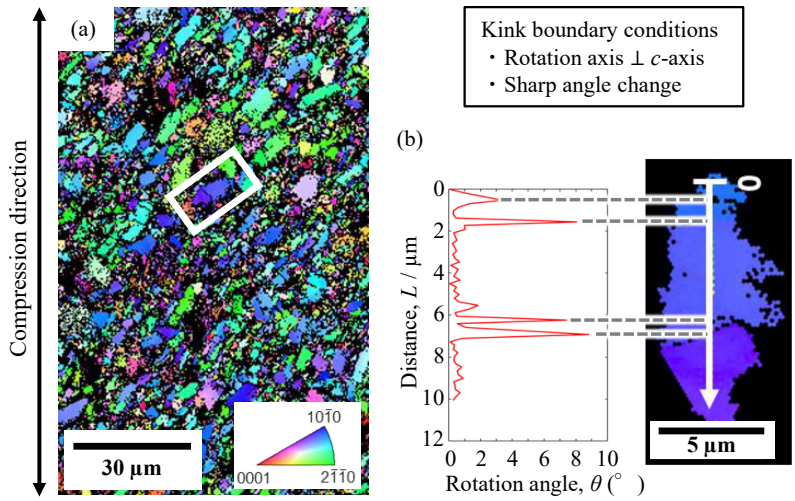

Fig. 9 Method of kink band analysis. (a) IPF map of sample. (b) Extracted IPF map of kinked grain surrounded by the white rectangular in (a) and rotation angle profile of the kinked grain. (online color)

Table 2 Difference in average number and average angle of kink boundaries (KBs) by the compression.

		Difference in average number of KBs (boundary/grain)	Difference in average angle of KBs (°)
Dense sample	$\varepsilon \fallingdotseq 10\%$	+0.10	-2.20
	$\varepsilon \fallingdotseq 20\%$	+0.30	-3.02
Low-porosity sample	$\varepsilon \fallingdotseq 10\%$	+0.25	-1.00
	$\varepsilon \fallingdotseq 20\%$	+0.24	-0.69
High-porosity sample	$\varepsilon \fallingdotseq 10\%$	+0.11	-3.40
	$\varepsilon \fallingdotseq 20\%$	-0.07	-0.47

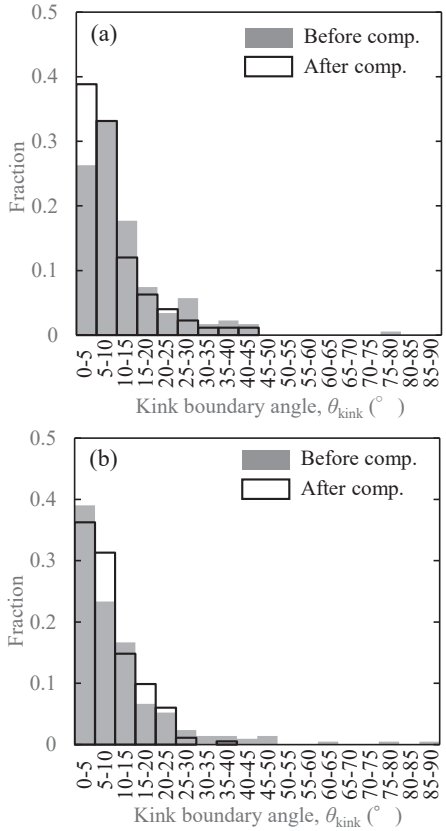

Fig. 10 Histograms of the kink boundary angles obtained from dense sample before (solid) and after (open) the compression. (a) intermediate sample, (b) large deformed sample.

In the High-porosity samples, the average number of kink boundaries initially increased and then decreased with further compression. This unique trend was not observed in the Dense or Low-porosity samples. Figure 11 shows a BSE image of the intermediately deformed High-porosity sample. Delamination and kink boundaries are indicated by the white and black arrows, respectively. This microstructure was only observed in the intermediately deformed sample. These results suggest that the formation and disappearance of tiny kink deformation bands may occur during high temperature compression of High-porosity samples, which exhibit high n-values. This mechanism may include the migration of preexisting kink boundaries, as well as the formation of TiC layers due to the diffusion of Ti and C and the evaporation of

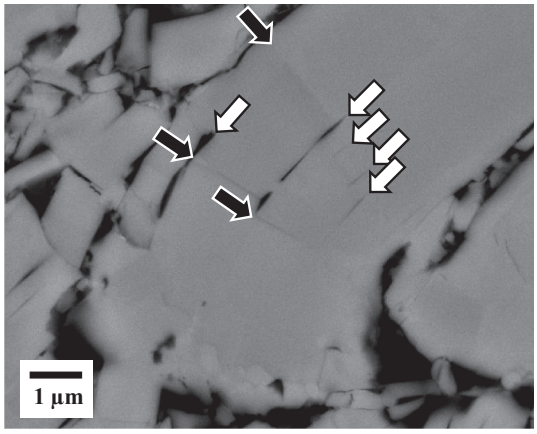

Fig. 11 BSE image of the intermediate compressive specimen of high-porosity sample tested. The black and white arrows show kink boundaries and delamination, respectively.

Si. The migration of such kink boundaries could induce delamination between the Ti ang Si layers, increasing the free energy of the samples due to new interfaces. To complement this increase, TiC layers could form via diffusion. The formation of these TiC layers would reduce the number of slip planes (Ti-Si interfaces), potentially inhibiting dislocation motion and contributing to higher strength. Although this phenomenon was observed only in the High-porosity samples, understanding it is crucial for clarifying kink deformation and kink-band strengthening.

4. Conclusion

To investigate the relationship between the compression behavior, porosity, and microstructure of Ti_3SiC_2, we fabricated Ti_3SiC_2 textured pressureless-sintered bodies and evaluated their microstructures. Furthermore, High temperature compression tests were performed on textured samples with different porosities, and obtained the following conclusions:

(1) By combining slip casting in a rotating magnetic field and pressureless sintering, textured Ti_3SiC_2 pressureless-sintered bodies with uniformly dispersed pores were successfully fabricated.

(2) The 0.2% proof stress of Ti_3SiC_2 decreases linearly with increasing porosity before compression. However, the work-hardening coefficient of the High-porosity samples was larger than that of the other samples. This can be attributed to densification during compression.

(3) Analysis of the kink deformation bands showed that the number of kink boundaries per grain increased and then decreased only in the High-porosity sample during compression, suggesting that this phenomenon may be important for clarifying kink-band strengthening.

Acknowledgments

This work was financially supported by JSPS KAKENHI (Grant Numbers JP21H00087, JP21H00110, and JP18H05482) and NIMS Joint Research Hub Program. A part of this work was also supported by “Advanced Research Infrastructure for Materials and Nanotechnology in Japan

(ARIM)" of the Ministry of Education, Culture, Sports, Science and Technology (MEXT). Proposal Numbers JPMXP1222HK0034 and JPMXP1223HK0061 (Hokkaido University). A part of this work was conducted at HBXL, a joint-use facility of Hokkaido University.

REFERENCES

[1] M.W. Barsoum: The $M_{N+1}AX_N$ Phases: A New Class of Solids, Prog. Solid State Chem. **28** (2000) 201–281.
[2] M. Radovic and M.W. Barsoum: MAX phases: Bridging the gap between metals and ceramics, Am. Ceram. Soc. Bull. **92** (2013) 20–27.
[3] J. Gonzalez-Julian: Processing of MAX phases: From synthesis to applications, J. Am. Ceram. Soc. **104** (2020) 659–690.
[4] Y. Shirakami, K. Ikeda, S. Miura, K. Morita, T.S. Suzuki and Y. Sakka: Orientation Dependence of Plastic Deformation Behavior and Fracture Energy Absorption Mechanism around Vickers Indentation of Textured Ti_3SiC_2 Sintered Body, J. Jpn. Soc. Powder Metallurgy **67** (2020) 607–614.
[5] Y. Shirakami, K. Ikeda, S. Miura, K. Morita, T.S. Suzuki and Y. Sakka: Orientation Dependence of Plastic Deformation Behavior and Fracture Energy Absorption Mechanism around Vickers Indentation of Textured Ti_3SiC_2 Sintered Body, Mater. Trans. **64** (2023) 650–656.
[6] Y. Shirakami, K. Ikeda, S. Miura, K. Morita, T.S. Suzuki and Y. Sakka: Orientation Dependence of High Temperature Compressive Behavior of Textured Ti_3SiC_2, Mater. Trans. **64** (2023) 805–812.
[7] E. Orowan: A type of plastic deformation new in metals, Nature **149** (1942) 643–644.
[8] J.B. Hess and C.S. Barrett: Structure and Nature of Kink Bands in Zinc, JOM **1** (1949) 599–606.
[9] M.W. Barsoum, A. Murugaiah, S.R. Kalidindi, T. Zhen and Y. Gogotsi: Kink bands, nonlinear elasticity and nanoindentations in graphite, Carbon **42** (2004) 1435–1445.
[10] I.A. Bell, C.J.L. Wilson, A.C. McLaren and M.A. Etheridge: Kinks in mica: role of dislocations and (001) cleavage, Tectonophysics **127** (1986) 49–65.
[11] I. Usov, G. Nyström, J. Adamcik, S. Handschin, C. Schütz, A. Fall, L. Bergström and R. Mezzenga: Understanding nanocellulose chirality and structure–properties relationship at the single fibril level, Nat. Commun. **6** (2015) 7564.
[12] M.W. Barsoum, L. Farber and T. El-Raghy: Dislocations, Kink Bands, and Room-Temperature Plasticity of Ti_3SiC_2, Metall. Mater. Trans. A **30** (1999) 1727–1738.
[13] M.W. Barsoum and T. El-Raghy: Room-Temperature Ductile Carbides, Metall. Mater. Trans. A **30** (1999) 363–369.
[14] D. Matsui, K. Morita, D. Terada, K. Ikeda and S. Miura: Kink Formation through Creep Deformation and Possibility of Kink Strengthening in Ti_3SiC_2–MAX Phase, J. Japan Inst. Met. Mater. **85** (2021) 439–448.
[15] D. Matsui, K. Morita, D. Terada, K. Ikeda and S. Miura: Kink Formation through Creep Deformation and Possibility of Kink Strengthening in Ti_3SiC_2 MAX Phase, Mater. Trans. **63** (2022) 1055–1064.
[16] M. Higashi, S. Momono, K. Kishida, N.L. Okamoto and H. Inui: Anisotropic plastic deformation of single crystals of the MAX phase compound Ti_3SiC_2 investigated by micropillar compression, Acta Mater. **161** (2018) 161–170.
[17] Y. Kawamura: Material Characteristics and Future Perspective on LPSO-type Magnesium Alloys, Materia Japan **54** (2015) 44–49.
[18] S. Yoshimoto, M. Yamasaki and Y. Kawamura: Microstructure and Mechanical Properties of Extruded Mg-Zn-Y Alloys with 14H Long Period Ordered Structure, Mater. Trans. **47** (2006) 959–965.
[19] H. Somekawa and D. Ando: Microstructure and mechanical properties of caliber rolled Mg–Y–Zn alloys, Mater. Sci. Eng. A **780** (2020) 139144.
[20] K. Hagihara, T. Tokunaga, S. Ohsawa, S. Uemichi, K. Guan, D. Egusa and E. Abe: Microstructural factors governing the significant strengthening of Al/Al_2Cu mille-feuille structured alloys accompanied by kink-band formation, Int. J. Plast. **158** (2022) 103419.
[21] N. Hashimoto, K. Ikeda, S. Miura, K. Morita, T.S. Suzuki and Y. Sakka: Fabrication of Textured Porous Ti_3SiC_2 by Slip Casting under High Magnetic Field and Microstructural Evolution through High Temperature Deformation, J. Japan Inst. Met. Mater. **85** (2021) 256–263.
[22] N. Hashimoto, K. Ikeda, S. Miura, K. Morita, T.S. Suzuki and Y. Sakka: Fabrication of Textured Porous Ti_3SiC_2 by Slip Casting under High Magnetic Field and Microstructural Evolution through High Temperature Deformation, Mater. Trans. **63** (2022) 133–140.
[23] Z. Jiang, S. Wang, X. Chen, W. Yang, X. Yao, X. Hu, Q. Han and H. Wang: Tape-Casting $Li_{0.34}La_{0.56}TiO_3$ Ceramic Electrolyte Films Permit High Energy Density of Lithium-Metal Batteries, Adv. Mater. **32** (2020) 1906221.
[24] T. Takenaka and K. Sakata: Grain Orientation and Electrical Properties of Hot-Forged $Bi_4Ti_3O_{12}$ Ceramics, Jpn. J. Appl. Phys. **19** (1980) 31–39.
[25] T.S. Suzuki, Y. Sakka and K. Kitazawa: Preferred Orientation of the Texture in the SiC Whisker-Dispersed Al_2O_3 Ceramics by Slip Casting in a High Magnetic Field, J. Ceram. Soc. Jpn. **109** (2001) 886–890.
[26] C.F. Hu, Y. Sakka, H. Tanaka, T. Nishimura and S. Grasso: Fabrication of Textured Nb_4AlC_3 Ceramic by Slip Casting in a Strong Magnetic Field and Spark Plasma Sintering, J. Am. Ceram. Soc. **94** (2011) 410–415.
[27] M. Mishra, Y. Sakka, C. Hu, T.S. Suzuki, T. Uchikoshi and L. Besra: Electrophoretic Deposition of Ti_3SiC_2 and Texture Development in a Strong Magnetic Field, J. Am. Ceram. Soc. **95** (2012) 2857–2862.
[28] C. Hu, Y. Sakka, S. Grasso, T. Suzuki and H. Tanaka: Tailoring Ti_3SiC_2 Ceramic via a Strong Magnetic Field Alignment Method Followed by Spark Plasma Sintering, J. Am. Ceram. Soc. **94** (2011) 742–748.
[29] K. Sato, M. Mishra, H. Hirano, T.S. Suzuki and Y. Sakka: Fabrication of textured Ti_3SiC_2 ceramic by slip casting in a strong magnetic field and pressureless sintering, J. Ceram. Soc. Jpn. **122** (2014) 817–821.
[30] T. El-Raghy, M.W. Barsoum, A. Zavaliangos and S.R. Kalidindi: Processing and Mechanical Properties of Ti_3SiC_2: II, Effect of Grain Size and Deformation Temperature, J. Am. Ceram. Soc. **82** (1999) 2855–2860.
[31] J.F. Li, W. Pan, F. Sato and R. Watanabe: Mechanical properties of polycrystalline Ti_3SiC_2 at ambient and elevated temperatures, Acta Mater. **49** (2001) 937–945.
[32] R.L. Coble and W.D. Kingery: Effect of Porosity on Physical Properties of Sintered Alumina, J. Am. Ceram. Soc. **39** (1956) 377–385.
[33] E. Ryshkewitch: Compression Strength of Porous Sintered Alumina and Zirconia, J. Am. Ceram. Soc. **36** (1953) 65–68.
[34] W. Duckworth: Discussion of Ryshkewitch Paper by Winston Duckworth, J. Am. Ceram. Soc. **36** (1953) 68.
[35] F.P. Knudsen: Dependence of Mechanical Strength of Brittle Polycrystalline Specimens on Porosity and Grain Size, J. Am. Ceram. Soc. **42** (1959) 376–387.
[36] L.J. Gibson: The mechanical behaviour of cancellous bone, J. Biomater. **18** (1985) 317–328.
[37] M. Hakamada, T. Kuromura, Y. Chino, Y. Yamada, Y. Chen, H. Kusuda and M. Mabuchi: Monotonic and cyclic compressive properties of porous aluminum fabricated by spacer method, Mater. Sci. Eng. A **459** (2007) 286–293.
[38] M. Hakamada, Y. Asao, T. Kuromura, Y. Chen, H. Kusuda and M. Mabuchi: Density dependence of the compressive properties of porous copper over a wide density range, Acta Mater. **55** (2007) 2291–2299.